Supporting Information

Consequences of Confinement for Alkene Epoxidation with Hydrogen Peroxide on Highly Dispersed Group 4 and 5 Metal Oxide Catalysts

Daniel T. Bregante,[1] Nicholas E. Thornburg,[2] Justin M. Notestein,[2] and David W. Flaherty[1,*]

[1]Department of Chemical and Biomolecular Engineering
University of Illinois Urbana-Champaign, Urbana, IL 61801

[2]Department of Chemical and Biological Engineering
Northwestern University, Evanston, IL 60208

*Corresponding Author

Phone: (217) 244-2816

Email: dwflhrty@illinois.edu

S1.0 Additional Catalyst Characterization and Verification of Measuring True Kinetics

S1.1 Catalyst Characterization

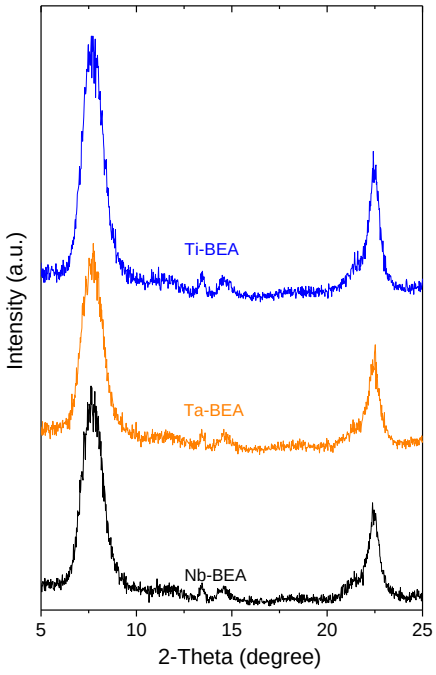

Figure S1. X-ray diffractograms for Ti- (blue), Nb- (black), and Ta-BEA (orange) taken on a Siemens/Bruker D5000 X-ray diffractometer with Cu Kα radiation (0.15418 nm) at ambient conditions. Reproduced from ref [1]. Copyright 2017 American Chemical Society.

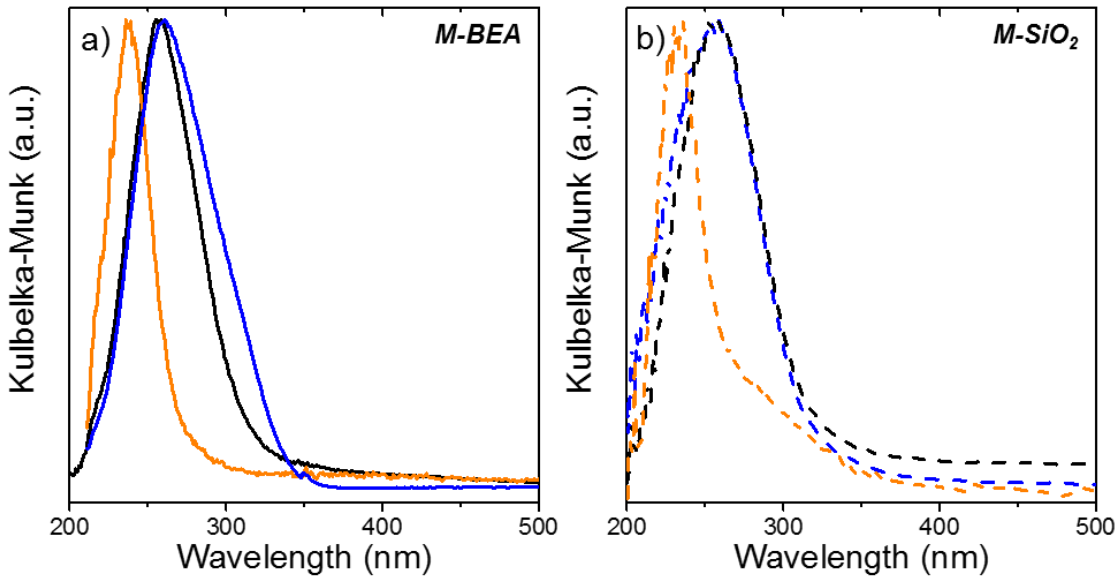

Figure S2. Diffuse reflectance UV-vis spectra for (a) M-BEA (solid lines) and (b) M-SiO_2 (dashed lines) catalysts. Colors represent: Ti (blue), Nb (black) and Ta (orange). (a) is reproduced with permissions from ref [1]. Copyright 2017 American Chemical Society.

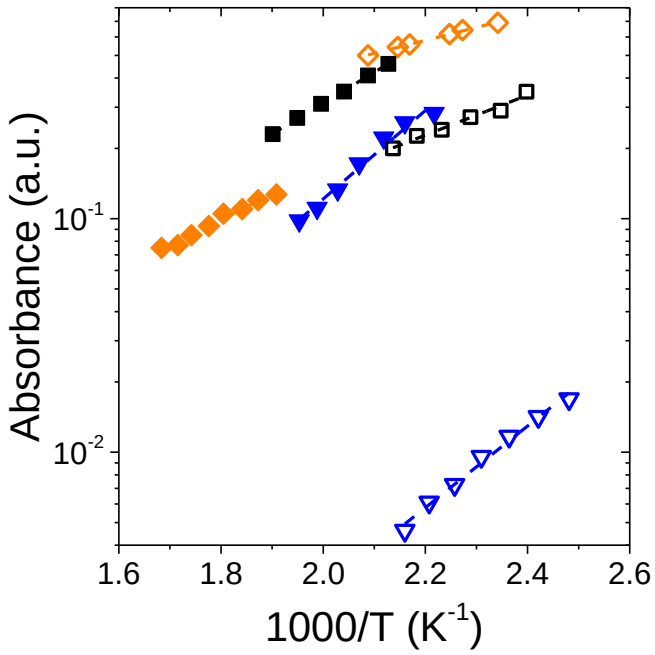

Figure S3. IR absorbance intensities for the Lewis-acid bound pyridine (~1450 cm^{-1} absorbance feature; Figure 1) on Ti-BEA (blue ▼, 1445 cm^{-1}), Nb-BEA (black ■, 1447 cm^{-1}), Ta-BEA (orange ♦, 1448 cm^{-1}), Ti-SiO_2 (blue open ▼, 1445 cm^{-1}), Nb-SiO_2 (black open ■, 1448 cm^{-1}), and Ta-SiO_2 (orange open ♦, 1449 cm^{-1}) as a function of inverse temperature (0.1 kPa pyridine, 101 kPa He, 50 cm^3 min^{-1}) after background subtraction. Dashed lines represent linear fits, where the slopes are proportional to the value of ΔH_{Py}.

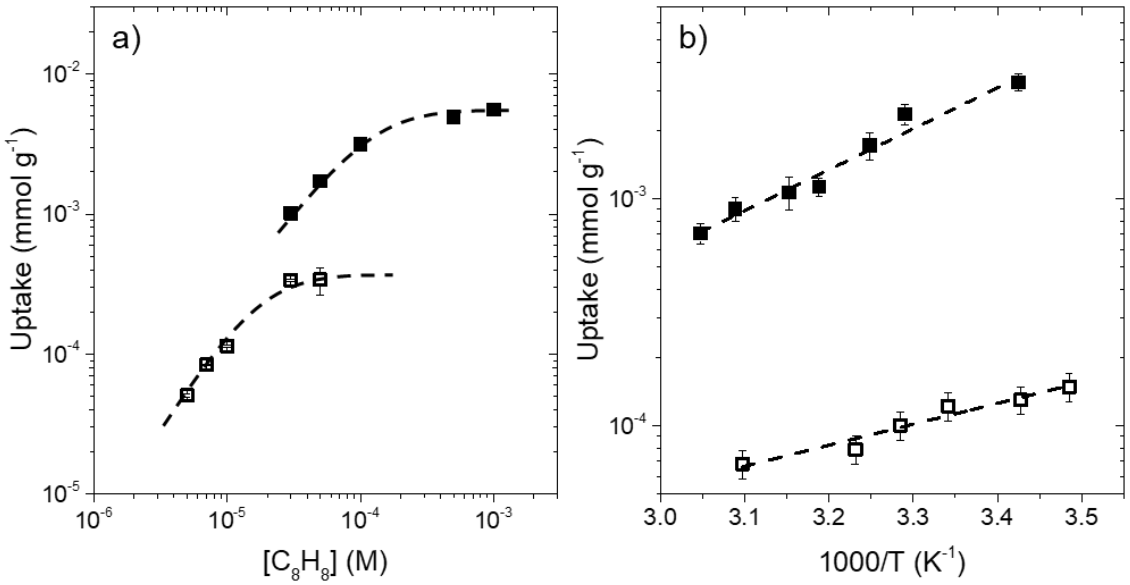

Figure S4. Styrene (C_8H_8) uptake (per gram of Si-BEA or SiO_2) into Si-BEA (solid symbols) and SiO_2 (open symbols) as a (a) function of [C_8H_8] (in CH_3CN, 313 K) and (b) inverse temperature (0.03 mM C_8H_8 for Si-BEA and 0.007 mM C_8H_8 for SiO_2 in CH_3CN). Dashed lines in Figure S4a are intended to guide the eye, while those in Figure S4b are linear fits where the slopes are proportional to ΔH_{Ads}.

Figure S4a shows two distinct regimes of C_8H_8 uptake into purely siliceous materials (i.e., Si-BEA and SiO_2), where at low [C_8H_8], uptake is proportional to the concentration of [C_8H_8] in the bulk solution and approaches a saturation value at relatively high [C_8H_8] (e.g., >0.03 mM for SiO_2). Adsorption enthalpies for C_8H_8 within a solution of CH_3CN (i.e., the solvent used for epoxidation in this study) are measured by van't Hoff analysis (Figure S4b) for the uptake of C_8H_8 into these materials. The uptake or C_8H_8 must be measured under the linear regime for C_8H_8 uptake (i.e., low [C_8H_8]) as a function of [C_8H_8] to avoid any artifacts that arise from saturation of the micropores of *BEA or mesopores of SiO_2.

S1.2 Methylphosphonic Acid Titrations to Determine Fraction of Active Metal in M-BEA Catalysts

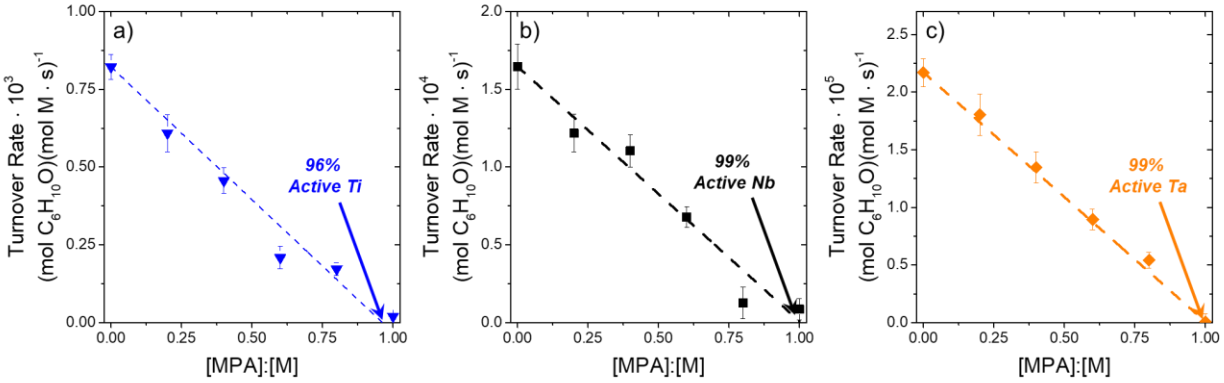

Figure S5. Turnover rates for $C_6H_{10}O$ formation as a function of methylphosphonic acid-to-metal ratio ([MPA]:[M]; 0.01 M C_6H_{10}, 0.01 M H_2O_2, 313 K) for (a) Ti-BEA, (b) Nb-BEA, and (c) Ta-BEA. Dashed lines represent linear regression fits with the y-intercept set to the turnover rate in the absence of the MPA titrant.

M-BEA was stirred with cyclohexene (0.01 M), benzene (an internal standard), CH_3CN (solvent), and an appropriate amount of methylphopshonic acid (MPA) at 313 K for 30 min with the intent of irreversibly adsorbing MPA to the active metal atoms. Epoxidations were initiated by the introduction of H_2O_2, and cyclohexene oxide ($C_6H_{10}O$) formation rates were determined using a gas chromatograph and analyzing extracted aliquots of the reaction mixture as a function of time. Figure S5 shows that turnover rates on M-BEA (M = Ti, Nb, and Ta) decrease linearly with the ratio of MPA:M, which suggests that the MPA selectively titrates the active sites for epoxidation. The extrapolation of these data to the point where turnover rates approach zero gives the fraction of metal atoms that are active for epoxidation.[2]

S.1.3 Control Experiments to Test Importance of Mass Transfer

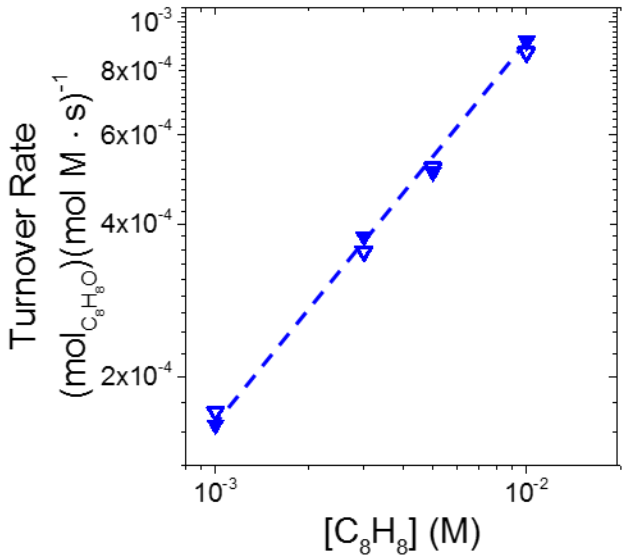

Figure S6. Turnover rates for the formation of C_6H_{10} measured as a function of $[C_6H_{10}]$ on Ti-BEA (blue solid ▼, 0.22 mmol Ti g^{-1}; 0.01 M H_2O_2, 313 K) and Ti-BEA (blue open ▼, 0.02 mmol Ti g^{-1}; 0.01 M H_2O_2, 313 K). Dashed line is intended to guide the eye.

Figure S5 shows rates for the formation of styrene oxide (C_8H_8O) via primary reaction pathways measured as a function of C_8H_8 concentration for multiple metal loadings of Ti (0.22 mmol g^{-1} and 0.02 mmol g^{-1}) in Ti-BEA. The rate of C_8H_8O formation is invariant with metal loading, which indicates that the Madon-Boudart criterion is satisfied for Ti-BEA.[3] Under the conditions tested, we see that the turnover rate for C_8H_8O formation is proportional to $[C_8H_8]$ and independent of $[H_2O_2]$, which corresponds to a simplified rate expression (Section 3.3 of main text) of:

$$\frac{r_E}{[L]} = k_4[C_8H_8] \tag{S1}$$

where r_E is the rate of $C_6H_{10}O$ formation, [L] is the total number of metal atoms in the reactor, k4 is the rate constant for step 4 of scheme 2, and $[C_8H_8]$ is the concentration of C_8H_8. For a first-order reaction (such as in equation S1), an effective Thiele modulus for a spherical pellet[3] can be defined as:

$$\phi = \left(\frac{k_4 R^2 [C_8H_8]}{D_e} \right)^{1/2} \tag{S2}$$

where ϕ is the Thiele modulous, R is the radius of the spherical pellet, $[C_8H_8]$ is the bulk concentration of C_8H_8, and D_e is the effective diffusivity of C_8H_8 through the spherical pellet. The Madon-Boudart criterion is an experimental way to determine the relative value of the Thiele

modulus, where the independence of turnover rates on metal loading signifies a relatively small Thiele modulus (i.e., $\phi << 1$). When the Thiele modulous is small, the rates of diffusion are much greater than those for the inherent kinetics of the reaction (at reactant concentrations equal to that in the bulk fluid phase), which shows that the measured reaction rates are not convoluted by diffusion restrictions within the catalyst particles.

In Figure 5 (main text), C_8H_8 formation rates are highest for Ti-BEA (of all M-BEA and M-SiO_2) under these conditions. Therefore all other M-BEA andM M-SiO_2 give values of k_3 that are much smaller than for Ti-BEA, which suggests that Thiele moduli on these materials are even smaller than that for Ti-BEA. Additionally, M-SiO_2 catalysts possess nominal pore diameters of 5.4 nm, which are significantly larger than those in M-BEA (~0.7 nm). This increases the effective diffusivity of C_8H_8 in M-SiO_2 materials relative to M-BEA and decreases the Thiele moduli further. Therefore, satisfaction of the Madon-Boudart criterion for Ti-BEA suggests that the other M-BEA and M-SiO_2 are also not mass-transfer limited and all measured reaction rates are reflective of only chemical kinetics.

S1.4 X-ray Photoelectron Spectroscopy of Untreated and H_2O_2-Treated M-BEA and M-SiO_2

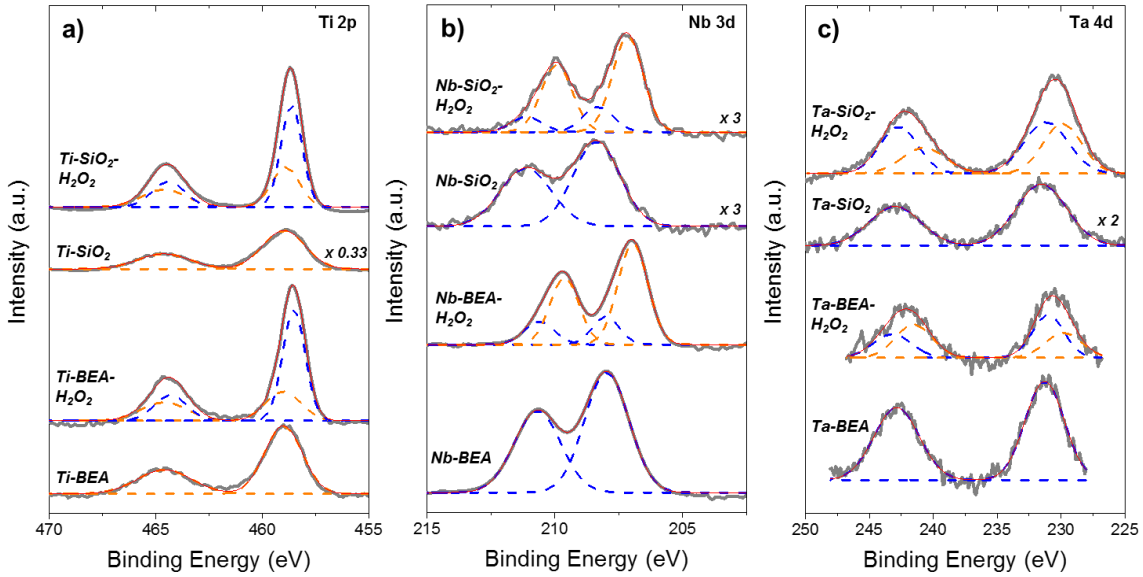

Figure S7. X-ray photoelectron spectra (gray, bold) of the (a) Ti 2*p*, (b) Nb 3*d*, and (c) Ta 4*d* regions on untreated and H_2O_2-treated (Section 2.2) Ti-, Nb-, and Ta- BEA and SiO_2. The peak fittings from the different oxidation states are color coded (blue and orange dashed curves) for clarity with the cumulative peak fit in red (solid). Table S1 contains peak center values and corresponding metal oxidation states. Spectra are references to an aliphatic C 1*s* feature at 284.8 eV. Nb-BEA data is adapted from ref [6].

Figure S7 shows X-ray photoelectron spectra that reveal the oxidation states of Ti, Nb, and Ta atoms in both untreated and H_2O_2-treated M-BEA and M-SiO_2. Untreated Ti-, Nb-, and Ta-materials possess doublet features that correspond to Ti^{4+} (Ti $2p_{1/2}$ and Ti $2p_{3/2}$),[4,5] Nb^{5+} (Nb $3d_{3/2}$ and Nb $3d_{5/2}$),[6,7] and Ta^{5+} (Ta $4d_{5/2}$ and Ta $4d_{7/2}$)[8] species, respectively, both in the *BEA framework and grafted onto SiO_2. Table S1 summarizes the position of the peak centers and corresponding oxidation states. In the case of Ti-BEA and Ti-SiO_2, treatment with H_2O_2 creates two additional features with peak binding energies that are ~ 0.3 eV lower than those of the untreated Ti-BEA and Ti-SiO_2 materials. The red shift of ~0.3 eV indicates that a fraction of the Ti atoms are coordinated to electron rich substituents, such as for Ti-(η^2-O_2) and Ti-OOH, after treatment with H_2O_2. Notably, these shifts are not large enough, however, to suggest a full formal oxidation state change from Ti^{4+} to Ti^{3+}.[5] Nb and Ta materials show overlapping features with significant shifts (~1 eV) in electron binding energies that may indicate a fraction of the metal cations reduce from a +5 to +4 oxidation state upon reaction with H_2O_2,[6,8] which may be due to the Haber-Weiss decomposition of M-OOH species to produce reduced metal centers,[9] or result from X-ray induced photoreduction of Nb and Ta metal centers.[10]

Table S1. Photoelectron Binding Energies (BE) and Corresponding Oxidation States of Metal Atoms in Untreated and H_2O_2-Activated M-BEA and M-SiO_2, as Determined by X-ray Photoelectron Spectroscopy.[a]

Sample	Untreated Samples BE (eV)	Untreated Samples Oxidation States	H_2O_2-activated Samples BE (eV)	H_2O_2-activated Samples Oxidation State(s)
Ti-BEA	464.7, 459.0	+4[b]	464.7, 459.0	+4[b]
			464.3, 458.5	+4[b]
Nb-BEA	210.6, 208.0	+5[c]	210.6, 208.0	+5[c]
			209.7, 207.0	+4[c]
Ta-BEA	243.0, 231.3	+5[d]	243.4, 231.0	+5[d]
			241.1, 229.7	+4[d]
Ti-SiO_2	464.6, 458.9	+4[b]	464.6, 458.9	+4[b]
			464.4, 458.6	+4[b]
Nb-SiO_2	211.1, 208.3	+5[c]	211.1, 208.3	+5[c]
			209.9, 207.1	+4[c]
Ta-SiO_2	243.0, 231.6	+5[d]	241.8, 231.1	+5[d]
			240.6, 229.8	+4[d]

[a]See Figure S7 for XP spectra; [b]Refs [3, 4]; [c]Refs [5, 6]; [d] Ref [7]

S2. Identification of Active Intermediates via *In Situ* UV-Visible and Raman Spectroscopy

S2.1 Sample Raw UV-Vis Spectrum and Method for Processing Spectra

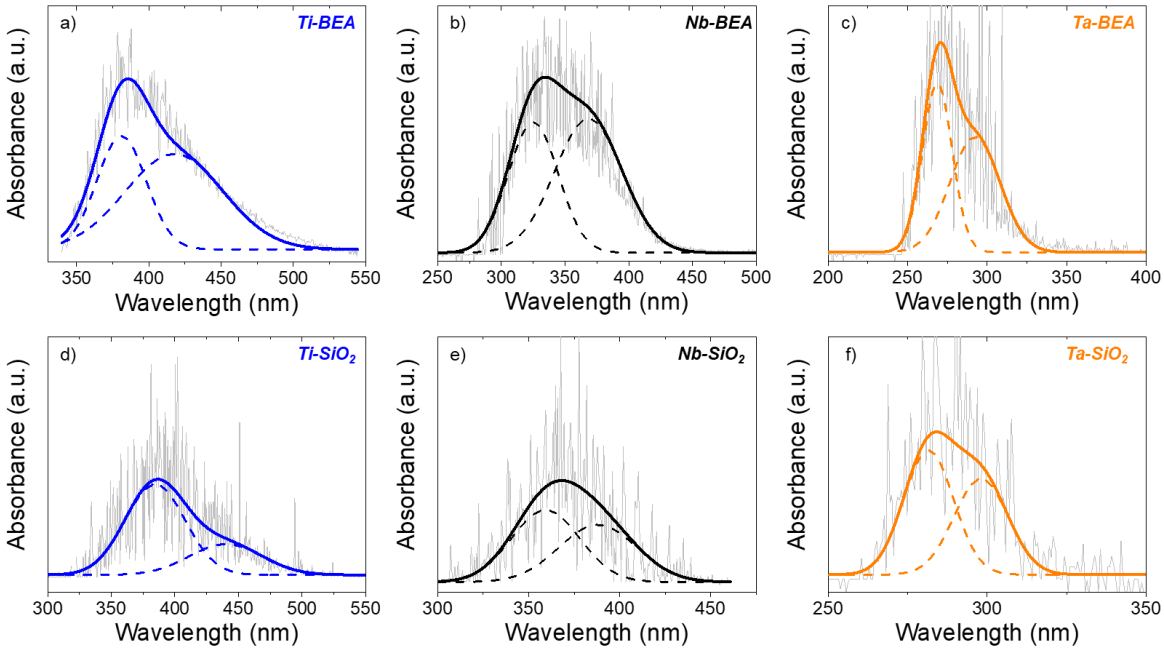

Figure S8. UV-vis absorbance spectrum (raw data, gray) of H_2O_2-treated (a) Ti-BEA, (b) Nb-BEA, (c) Ta-BEA, (d) Ti-SiO_2, (e) Nb-SiO_2, and (f) Ta-SiO_2 at 313 K in flowing CH_3CN (0.4 M H_2O) and smoothed data (bold black line) using a finite fourier transform (20 points of smoothing). Dashed curves represent peak fittings using a Gaussian function.

S2.2 Values of Ligand to Metal Charge Transfer Energies for H_2O_2-activated M-BEA and M-SiO_2

Table S2. Ligand to Metal Charge Transfer Energies (hν) for the M-OOH and M-(η^2-O_2) Intermediates as Detected via *In Situ* UV-vis Spectra (Figure 2).

Material	LMCT hν (eV) for M-OOH	LMCT hν (eV) for M-(η^2-O_2)
Ti-BEA	2.95	3.25
Nb-BEA	3.48	3.99
Ta-BEA	4.21	4.54
Ti-SiO_2	2.81	3.25
Nb-SiO_2	3.36	3.65
Ta-SiO_2	4.11	4.38

S2.3 Time-Resolved *In Situ* UV-Vis Spectroscopy and Kinetic Parameter Optimization

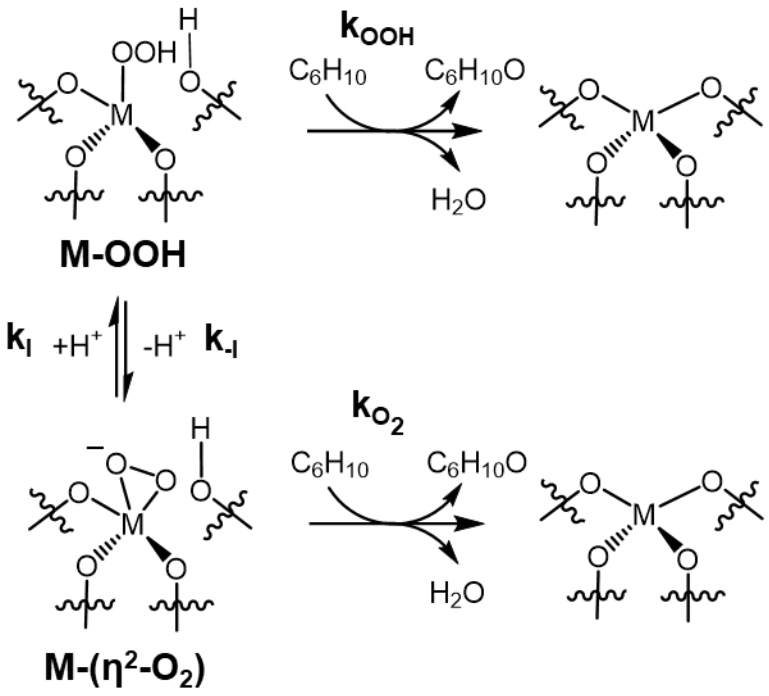

Scheme 1 (copied from main text). Consumption and interconversion of M-OOH and M-(η^2-O_2) species upon reaction with C_6H_{10} on group 4 metals.

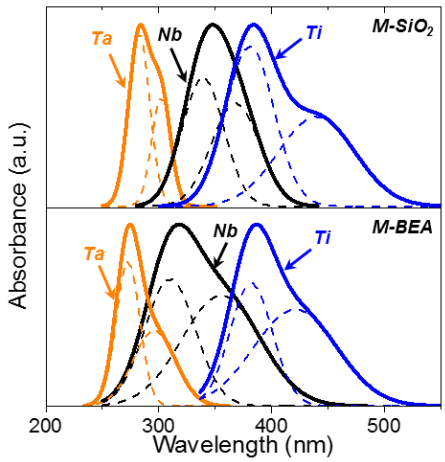

Figure 2 (copied from main text). UV-vis spectra of H_2O_2-activated M-SiO_2 (top) and M-BEA (bottom) materials. Spectra were acquired in situ in flowing H_2O_2 in CH_3CN (0.1 M H_2O_2, 0.4 M H_2O, 1 cm^3 min^{-1}) at 313 K. Different colors indicate: Ta (orange), Nb (black), and Ti (blue), and dashed lines represent deconvoluted Gaussian peaks for M-(η^2-O_2) and M-OOH species.

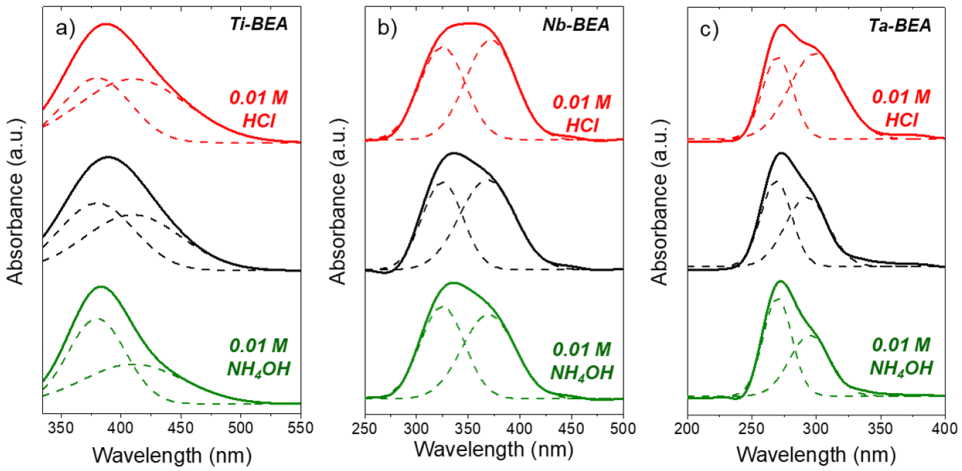

Figure 3 (copied from main text). UV-vis spectra of H_2O_2-activated (a) Ti-BEA, (b), Nb-BEA, and (c) Ta-BEA. Spectra were acquired in situ in flowing H_2O_2 in CH_3CN (0.1 M H_2O_2, 0.4 M H_2O, 1 cm^3 min^{-1}; black), with HCl (0.01 M HCl, 0.1 M H_2O_2, 0.4 M H_2O, 1 cm^3 min^{-1}; red) or NH_4OH (0.01 M NH_4OH, 0.1 M H_2O_2, 0.4 M H_2O, 1 cm^3 min^{-1}; green) at 313 K. Dashed lines represent Gaussian peak fits for M-(η^2-O_2) and M-OOH species.

The change in surface coverage of the M-OOH and M-(η^2-O_2) species depends on the summed rates of formation/consumption through interconversion and consumption by reaction with C_6H_{10}, which take the forms of:

$$\frac{d[M-(\eta^2-O_2)]}{dt} = k_{-I}[M-OOH] - k_I[M-(\eta^2-O_2)] - k_{O_2}[M-(\eta^2-O_2)][C_6H_{10}] \quad \text{(S3)}$$

$$\frac{d[M-OOH]}{dt} = k_I[M-(\eta^2-O_2)] - k_{-I}[M-OOH] - k_{OOH}[M-OOH][C_6H_{10}] \quad \text{(S4)}$$

where [M-OOH] and [M-(η^2-O_2)] represent the coverages (assumed to be proportional to UV-vis absorbance feature intensities) of M-OOH and M-(η^2-O_2), respectively, and k_x is the rate constant for step x in scheme 1. Pseudo first-order kinetics are assumed for the reaction between M-(O_2) intermediates and C_6H_{10}, as throughout the experiment the ratio of [C_6H_{10}] to number of metal atoms exceeds 10^5 in all cases. Similarly, pseudo first-order kinetics are assumed for the interconversion (via protonation or deprotonation) of M-OOH and M-(η^2-O_2), as this process is likely mediated by nearby H_2O molecules (where [H_2O] was kept constant at 0.4 M).

The equilibrium coefficient (K_I) for the interconversion between M-OOH and M-(η^2-O_2) must be determined to constrain the ratio of k_I to k_{-I} and is defined as

$$K_I = \frac{k_I}{k_{-I}} = \frac{[M-OOH]}{[M-(\eta^2-O_2)]} = \frac{\varepsilon_{M-OOH}A_{M-OOH}}{\varepsilon_{M-(\eta^2-O_2)}A_{M-(\eta^2-O_2)}} \quad \text{(S5)}$$

where ε_{M-OOH} and $\varepsilon_{M-(\eta^2-O_2)}$ are the extinction coefficients (i.e., sensitivity factors) for M-OOH and M-(η^2-O_2), respectively, and A_{M-OOH} and $A_{M-(\eta^2-O_2)}$ are the areas of the steady-state UV-vis features (Figure 2) that correspond to M-OOH and M-(η^2-O_2) species, respectively. Equation S5 shows that the ratio of ε_{M-OOH} to $\varepsilon_{M-(\eta^2-O_2)}$ must be known to experimentally determine a value of K_I for a given catalyst.

The area of the cumulative UV-vis feature (A_{Total}) for a given M-BEA or M-SiO_2 (Figure 2) is given by

$$A_{Total} = A_{M-OOH} + A_{M-(\eta^2-O_2)} \tag{S6}$$

The total number of metal atoms ([M]) that are detected by the UV-vis spectroscopy are given by

$$[M] = \varepsilon_{M-OOH} A_{M-OOH} + \varepsilon_{M-(\eta^2-O_2)} A_{M-(\eta^2-O_2)} \tag{S7}$$

such that [M] is equal to the sum of the number of M-OOH and M-(η^2-O_2) intermediates. Equations S6 and S7 are then combined to linearize the A_{Total} as a function of $A_{M-(\eta^2-O_2)}$ to yield

$$A_{Total} = \frac{[M]}{\varepsilon_{M-OOH}} + (1 - \frac{\varepsilon_{M-(\eta^2-O_2)}}{\varepsilon_{M-OOH}}) A_{M-(\eta^2-O_2)} \tag{S8}$$

The peak areas within Figure 3 for the cumulative UV-vis feature and the UV-vis peak that is attributed to M-(η^2-O_2) can then be used to determine the ratio of ε_{M-OOH} to $\varepsilon_{M-(\eta^2-O_2)}$. Collection of UV-vis features under varying conditions (e.g., different acid and base solutions) is necessary to estimate the ratio of ε_{M-OOH} to $\varepsilon_{M-(\eta^2-O_2)}$ because this ratio depends on shifting the equilibrium between the M-OOH and M-(η^2-O_2) species while assuming that the total number of sites within the measurement is unchanged.

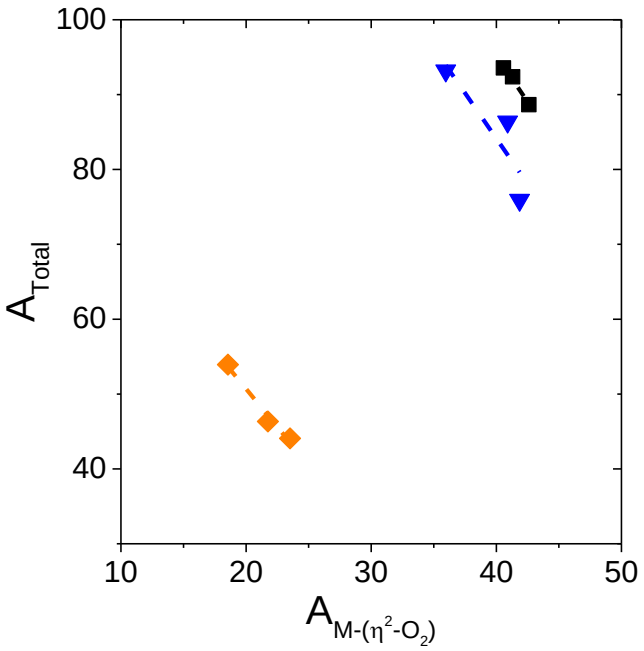

Figure S9. Total area (A_{Total}) as a function of $A_{M-(\eta^2-O_2)}$ for Ti- (blue ▼), Nb- (black ■), and Ta-BEA (orange ♦). Peak areas are from the steady-state UV-vis spectra (Figure 3) of these M-BEA materials when contacted with varying solutions of H_2O_2 with HCl and NH_4OH in CH_3CN (313 K). Dashed lines represent linear regression fits.

Figure S9 shows A_{Total} as a function of $A_{M-(\eta^2-O_2)}$ for all M-BEA materials, where the slope of each line is given by -2.42, -2.47, and -2.04 for Ti-, Nb-, and Ta-BEA respectively. From these slopes, equation S8 shows that the ratio of ε_{M-OOH} to $\varepsilon_{M-(\eta^2-O_2)}$ are 1.42, 1.47, and 1.04 for Ti-, Nb-, and Ta-BEA, respectively. These ratios of ε_{M-OOH} to $\varepsilon_{M-(\eta^2-O_2)}$, in conjunction with equation S5, are then used to determine values of k_I for each M-BEA and M-SiO_2 (Table S3).

MATLAB™ is used to numerically estimate the kinetic parameters, by fitting the data (Figure 4) to the coupled differential equations (eqns. S3 and S4). The initial guesses used for the rate constants were 0.01, 0.001, 0.001 for k_{-I}, k_{OOH}, and $k_{O_2^-}$, respectively. Values of k_I are constrained by the relationship between K_I and k_{-I} as shown in Equation S5. Changes of the initial values by an order of magnitude (increasing and decreasing) did not change the optimized parameter values.

Table S3. Numerically Optimized Rate Constants from Figure 4 (main text), k_i (s^{-1}), and Equilibrium Constants for the Interconversion of M-OOH and M-(η^2-O_2) (Scheme 1) and the Ratio of Rate Constants for M-OOH to M-(η^2-O_2) Reaction with C_6H_{10}.

Sample	k_{-I} (s^{-1})	k_I (s^{-1})	$k_{OOH} : k_{O_2}$	K_I
Ti-BEA	2.2×10^{-4}	2.0×10^{-4}	1.7	0.9
Nb-BEA	1.9×10^{-4}	2.1×10^{-4}	0.6	1.1
Ta-BEA	7.9×10^{-5}	7.9×10^{-5}	0.6	1.0
Ti-SiO_2	1.3×10^{-4}	2.2×10^{-4}	11.1	1.7
Nb-SiO_2	1.5×10^{-4}	2.6×10^{-4}	0.4	1.7
Ta-SiO_2	5.0×10^{-4}	8.3×10^{-4}	0.5	1.7

S2.4 Additional Raman Spectra of H_2O_2-Activated Ti-BEA

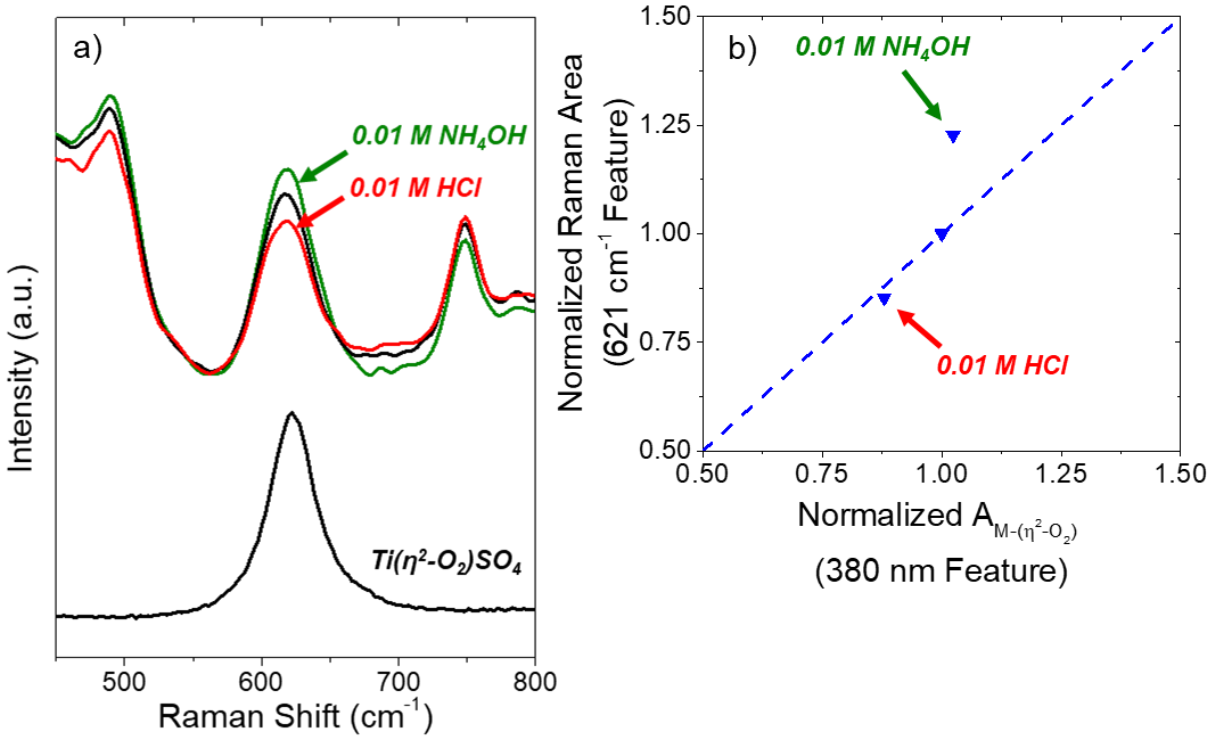

Figure S10. (a) Raman spectra of H_2O_2-activated Ti-BEA (top) and $TiOSO_4$ (to form Ti(η^2-O_2)SO_4; bottom) (λ_{ex} = 442 nm, 90 mW) and (b) correlation of the normalized 621 cm^{-1} feature peak areas to the normalized area of the UV-vis feature corresponding to Ti-(η^2-O_2) in Figure S9 when collected under identical reaction conditions. Ti-BEA Raman spectra were acquired in situ in flowing H_2O_2 in CH_3CN (0.1 M H_2O_2, 0.4 M H_2O, 1 cm^3 min^{-1}; black), with HCl (0.01 M HCl, 0.1 M H_2O_2, 0.4 M H_2O, 1 cm^3 min^{-1}; red) or NH_4OH (0.01 M NH_4OH, 0.1 M H_2O_2, 0.4 M H_2O, 1 cm^3 min^{-1}; green) at 313 K). Dashed line in Figure S10b represents parity.

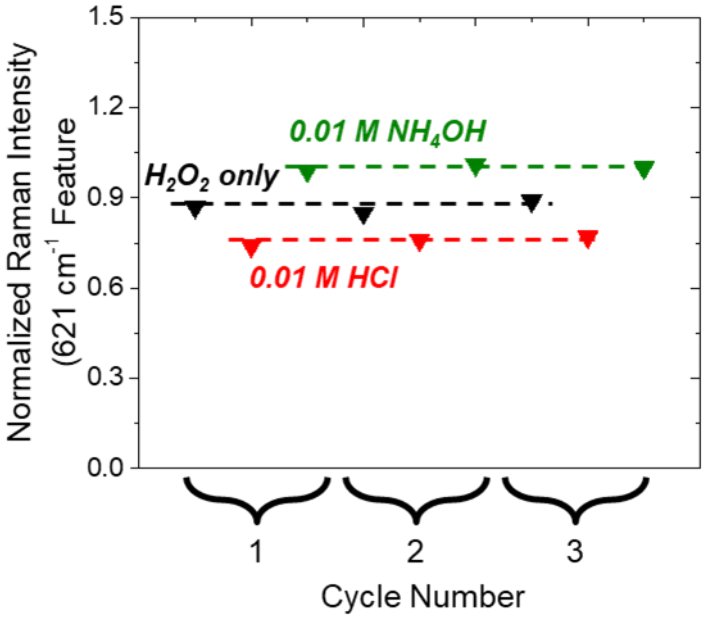

Figure S11. Steady-State peak intensities for the 621 cm^{-1} Raman feature (Figure S10) as a function of cycle number while switching from a flow of H_2O_2 in CH_3CN (0.1 M H_2O_2, 0.4 M H_2O, 1 cm^3 min^{-1}; black) to HCl (0.01 M HCl, 0.1 M H_2O_2, 0.4 M H_2O, 1 cm^3 min^{-1}; red) and finally NH_4OH (0.01 M NH_4OH, 0.1 M H_2O_2, 0.4 M H_2O, 1 cm^3 min^{-1}; green) at 313 K. Dashed lines are intended to guide the eye.

S3.0 Additional Kinetic Data, Derivation of Relevant Rate Expressions and Transition State Theory

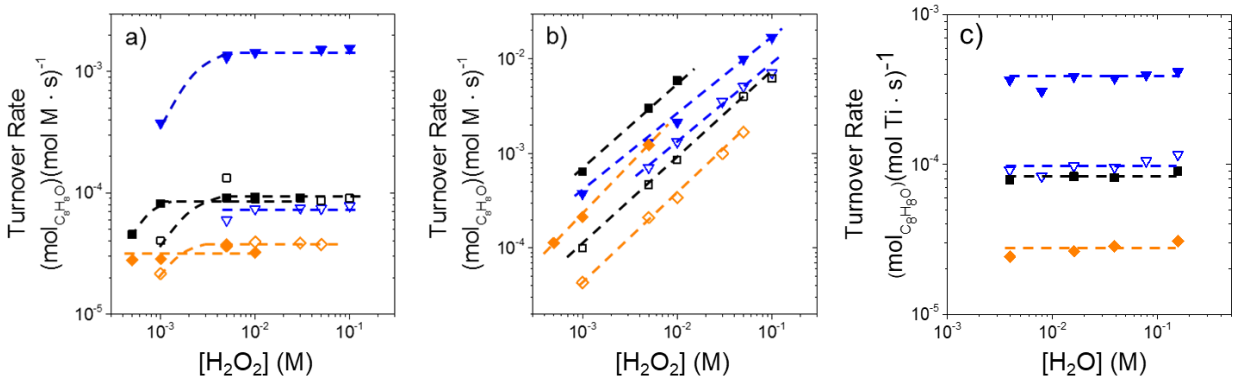

Figure S12. Turnover rates for the formation of styrene oxide via primary reaction pathways as a function of [H_2O_2] and [H_2O] for M-BEA (closed symbols) and M-SiO_2 (open symbols) at (a) 3 mM C_8H_8 (in CH_3CN, 313 K), (b) 0.5 M C_8H_8 (in CH_3CN, 313 K), and (c) 3 mM C_8H_8, 10 mM H_2O_2 (in CH_3CN, 313 K). Symbols and colors represent Ti- (blue ▼), Nb- (black ■) and Ta- (orange ♦) materials. Dashed lines are intended to guide the eye.

S3.1 Derivation of Full Rate Expression for C_8H_8 Epoxidation

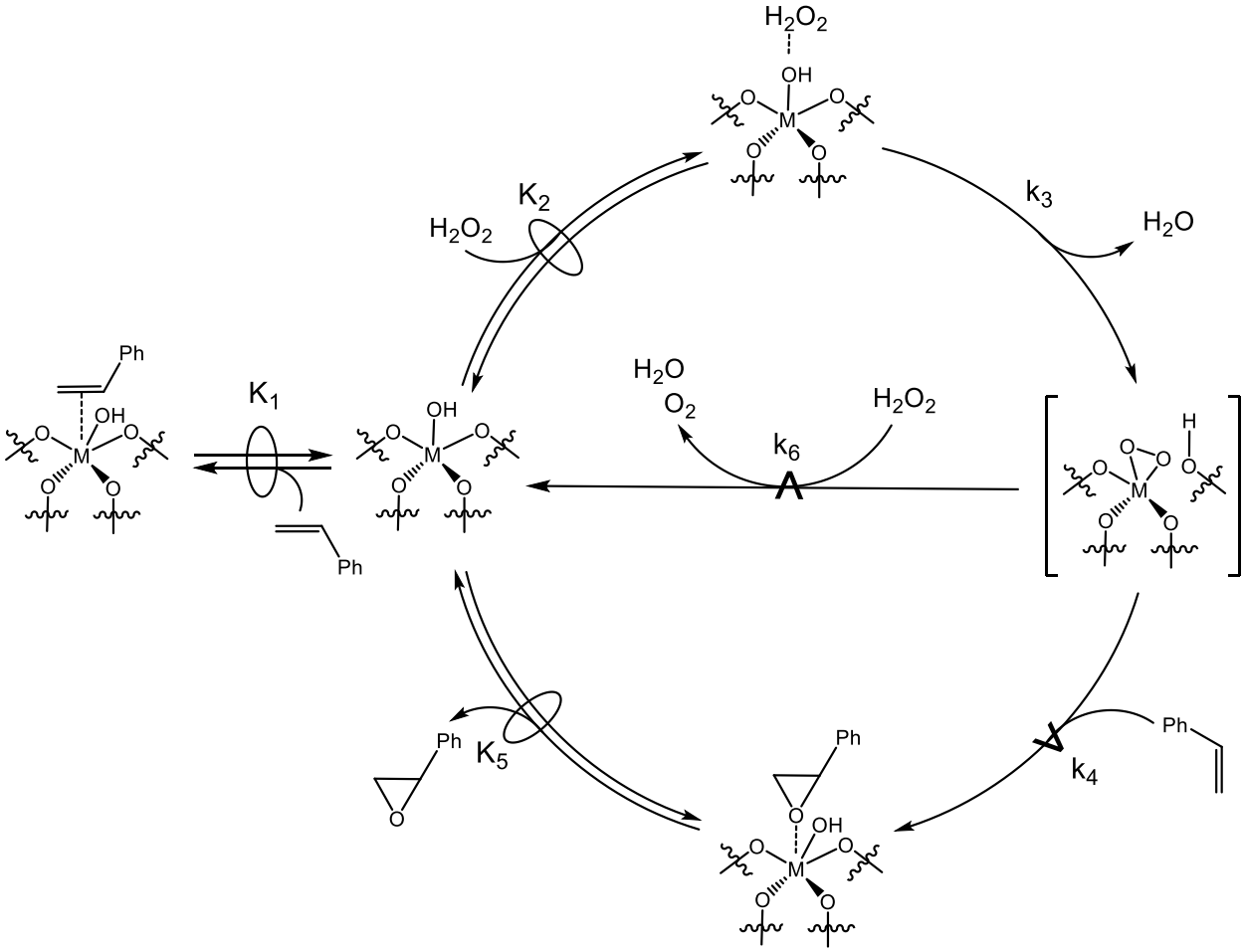

Scheme S1. Proposed Elementary Steps for C_8H_8 Epoxidation and H_2O_2 Decomposition over group 5 M-BEA and M-SiO_2 Catalysts. The symbol ⇄ represents a quasi-equilibrated step, while → represents a kinetically relevant step. Note, the depiction of M-(η^2-O_2) and adsorbed- C_8H_8, H_2O_2, and C_8H_8O are meant to represent different types of surface species, rather than suggest a specific type of coordination to the active catalytic site. The M-(η^2-O_2) intermediates drawn are intended to represent the pool of M-OOH and M-(η^2-O_2) species that are present as shown by UV-vis (Figure 2).

Scheme 2 shows a series of elementary steps that account for the measured effects of [C_8H_8] (Figure 5) and [H_2O_2] (Figure S10) on both rates of C_8H_8 epoxidation. The catalytic cycle involves the quasi-equilibrated adsorption of H_2O_2 (step 2),[3,7,11] followed by the irreversible activation of H_2O_2 (step 3) to form a pool of M-(η^2-O_2) (Nb and Ta)[7] and M-OOH (Ti)[12-15] active intermediates (referred to collectively as M-(O_2)), which then react with C_8H_8 to form C_8H_8O (step 4), followed by C_8H_8O desorption (step 5) or decompose by reaction with H_2O_2 (step 6). Measured C_8H_8 epoxidation rates represent the kinetically relevant reaction of the active form of the oxidizing surface intermediate with a C_8H_8 molecule:

$$r_E = k_4[M-(O_2)][C_8H_8] \tag{S9}$$

where r_E is the rate of C_6H_{10} epoxidation, [M-(O_2)] is the collective coverage of M-OOH (group IV) and M-(η^2-O_2) (group V) species, k_x is the rate constant for step x in Scheme 2, and [C_8H_8] is the concentration of C_8H_8. Application of the pseudo-steady state hypothesis to the M-(O_2) intermediates, results in:

$$r_E = \frac{k_3 k_4 K_2 [C_8H_8][H_2O_2][*]}{(k_4[C_8H_8] + k_6[H_2O_2])} \tag{S10}$$

where K_x is the equilibrium constant for step x and [*] is the total number of sites occupied by the solvent molecule (i.e., CH_3CN). An expression for [*] is given by the summation of all likely surface-bound intermediates:

$$[L] = [*] + [C_8H_8*] + [H_2O_2*] + [M-(O_2)] + [C_8H_8O*] \tag{S11}$$

where [L] is the total number of M atoms, [M-(O_2)] is the pool of M-OOH and M-(η^2-O_2) intermediates, and [C_8H_8*], [H_2O_2*], and [C_8H_8O*] are surface-bound C_8H_8, H_2O_2, and C_8H_8O molecules, respectively. Equation S11 can then be restated in terms of the rate and equilibrium constants, as well as liquid-phase reactant concentrations and unoccupied M atoms by application of the PSSH to each surface specie to yield:

$$[L] = [*] + K_1[C_8H_8][*] + K_2[H_2O_2][*] + \frac{k_3 K_2 [H_2O_2][*]}{(k_4[C_8H_8] + k_6[H_2O_2])} + K_5[C_8H_8O][*] \tag{S12}$$

Substitution of equation S12 into S10 yields the full rate expression for $C_6H_{10}O$ formation:

$$\frac{r_E}{[L]} = \frac{\dfrac{k_3 k_4 K_2 [C_8H_8][H_2O_2]}{(k_4[C_8H_8] + k_6[H_2O_2])}}{1 + K_1[C_8H_8] + K_2[H_2O_2] + \dfrac{k_3 K_2 [H_2O_2]}{(k_4[C_8H_8] + k_6[H_2O_2])} + K_5[C_8H_8O]} \tag{S13}$$

which is consistent with equation 2 from the main text.

Table S4. Calculated ratios of $k_4[C_8H_8]:k_6[H_2O_2]$ using interpolated values from Figure 5 and H_2O_2 decomposition rates at conditions that result in a C_8H_8O MARI (i.e., 0.5 M $[C_8H_8]$ and values of $[H_2O_2]$ used in Figure 5).

Sample	$k_4[C_8H_8]:k_6[H_2O_2]$
Ti-BEA	6.7
Nb-BEA	5.2
Ta-BEA	6.0
Ti-SiO_2	5.0
Nb-SiO_2	12.7
Ta-SiO_2	120.2

S3.2 Transition State Theory for Measurement of Activation Enthalpies and Entropies

Transition state theory (TST) is used to relate the stability of the reference state (e.g., the M-(O_2) intermediates) to an activated complex that leads to reaction (i.e., the transition state).[7,16,17] TST, when combined with our proposed mechanism (Scheme 2), proposes that the reactant species (i.e., M-(O_2), H_2O_2, and C_8H_8) exist in equilibrium with the transition state to yield:

$$\frac{r_E}{[L]} = \frac{k_B T}{h} K_E^{\ddagger}[C_8H_8] \tag{S14}$$

$$\frac{r_E}{[L]} = \frac{k_B T}{h} K_D^{\ddagger}[H_2O_2] \tag{S15}$$

where k_B is Boltzmann's constant, h is Planck's constant, T is the temperature in Kelvin, $K_E^{\ddagger}$ and $K_D^{\ddagger}$ are the Transition state equilibrium constants for epoxidation and H_2O_2 decomposition, respectively, and [C_8H_8] is the concentration of C_8H_8. Values of $K_E^{\ddagger}$ and $K_D^{\ddagger}$ may be expressed in terms of changes in Gibbs free energy, via the Eyring equation, to result in:

$$K_x^{\ddagger} = e^{-\Delta G_x^{\ddagger}/RT} = e^{-\Delta H_x^{\ddagger}/RT} e^{\Delta S_x^{\ddagger}/R} \tag{S16}$$

Where R is the ideal gas constant and $\Delta G^{\ddagger}$, $\Delta H^{\ddagger}$, and $\Delta S^{\ddagger}$ is the Gibb's free energy, enthalpy, and entropy of activation, respectively. Figure S11 shows measured values for $K_E^{\ddagger}$ and $K_D^{\ddagger}$ as a function of inverse temperature for all M-BEA and M-SiO_2.

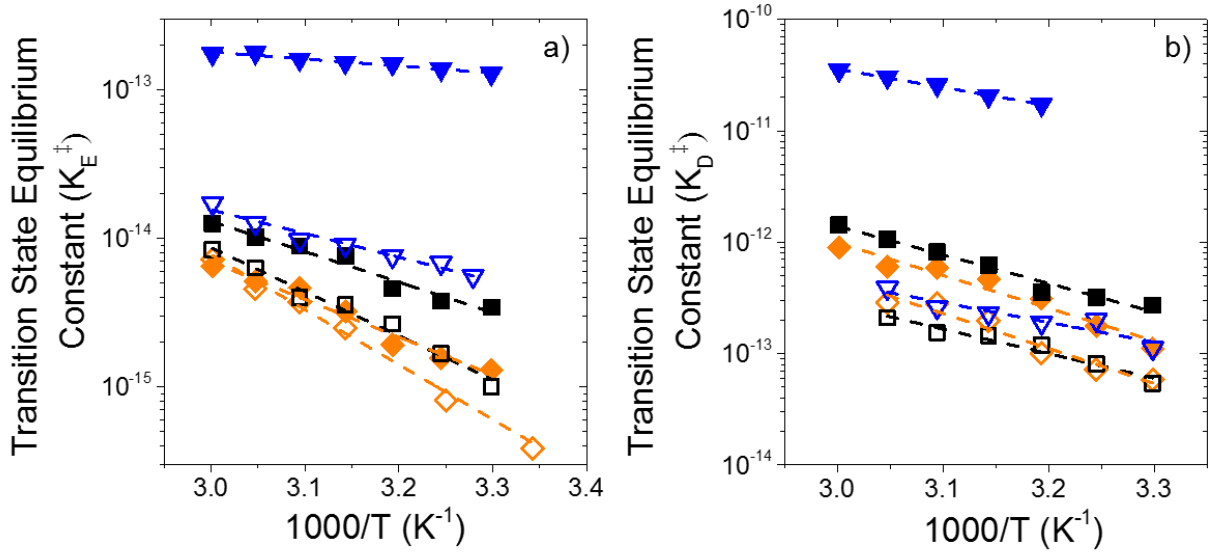

Figure S13. Transition state equilibrium constants for (a) C_8H_8 epoxidation ($K_E^{\ddagger}$) and (b) H_2O_2 decomposition ($K_D^{\ddagger}$) as functions of inverse temperature on M-BEA (closed symbols) and M-SiO_2 (open symbols). Reactions conditions: Ti-BEA (3 mM C_8H_8, 0.01 M H_2O_2), Nb-BEA (3 mM C_8H_8, 1 mM H_2O_2), Ta-BEA (3 mM, 1 mM H_2O_2), Ti-SiO_2 (3 mM C_8H_8, 0.01 M H_2O_2), Nb-SiO_2 (3 mM C_8H_8, 0.01 M H_2O_2), and Ta-SiO_2 (3 mM C_8H_8, 0.01 M H_2O_2). Symbols and colors represent Ti- (blue ▼), Nb- (black ■) and Ta- (orange ♦) materials. Error bars were omitted for clarity. In all reported data, error was < 7%. Dashed lines represent fits to the Eyring equation (equation S16) whose slopes and intercepts are proportional to $\Delta H^{\ddagger}$ and $\Delta S^{\ddagger}$, respectively.

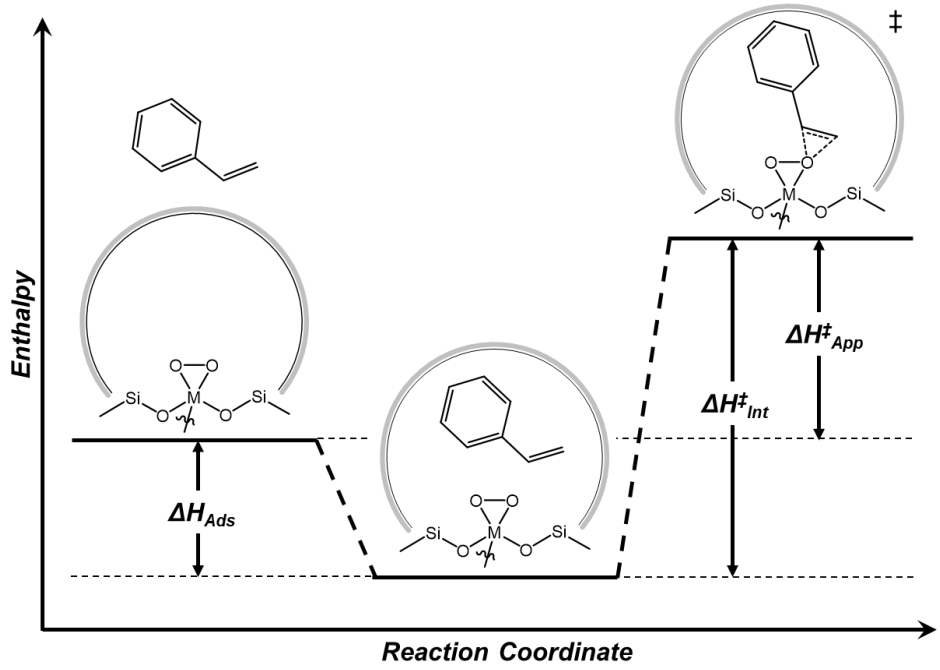

Scheme S2. Changes in Enthalpies Due to the Intermediate Steps that Form the Transition State for C_8H_8 Epoxidation from a M-(O_2) Saturated Surface and Fluid-Phase C_8H_8.[a] M-(η^2-O_2) (M = Nb or Ta) is shown to illustrate the relationship between $\Delta H^{\ddagger}_{App}$, ΔH_{Ads}, and $\Delta H^{\ddagger}_{Int}$. This thermochemical sequence for the epoxidation of C_8H_8 with a M-(η^2-O_2) reference state (i.e., M-(η^2-O_2) MASI) uses a transition state theory formalism that involves the quasi-equilibrated adsorption of C_8H_8 into the pores of *BEA or SiO_2, and the kinetically-relevant reaction of C_8H_8 with M-(η^2-O_2).

S4.0 Calculated Reaction Constants for the Epoxidation of *Para*-substituted Styrene

Table S5. Reaction Constants (ρ) for the Epoxidation of x-C_8H_7 (x = -NO_2, -Br, -H, -Me, or -OMe) on M-BEA and M-SiO_2 Materials at Standard Reaction Conditions ((3 mM x-C_8H_8, 0.01 M H_2O_2, in CH_3CN, 313 K). Values of ρ Represent Least Squares Regression Fits of the Hammett Equation (Equation 9 in the main text) to Figure 9.

Sample	Reaction constant (ρ)
Ti-BEA	-0.83
Nb-BEA	-0.80
Ta-BEA	-0.89
Ti-SiO_2	-0.91
Nb-SiO_2	-0.98
Ta-SiO_2	-0.93

References:

1. Bregante, D. T.; Flaherty, D. W. Periodic Trends in Olefin Epoxidation over Group IV and V Framework-Substituted Zeolite Catalysts: A Kinetic and Spectroscopic Study. *J. Am. Chem. Soc.* **2017**, *139*, 6888-6898.

2. Eaton, T. R.; Boston, A. M.; Thompson, A. B.; Gray, K. A.; Notestein, J. M., Counting Active Sites in Titanium Oxide-Silica Catalysts for Hydrogen Peroxide Activation Through In Situ Poisoning with Phenylphosphonic Acid. *ChemCatChem* **2014**, *6*, 3215-3222.

2. Madon, R. J.; Boudart, M., Experimental Criterion for the Absence of Artifacts in the Measurement of Rates of Heterogeneous Catalytic Reactions. *Ind. Eng. Chem. Fundam.* **1982**, *21*, 438-447.

3. Diebold, U.; Madey, T. E., TiO_2 by XPS. *Surf. Sci. Spectra* **1996**, *4*, 227-231.

4. Kurtz, R. L.; Henrich, V. E., Comparison of Ti 2p Core-Level Peaks from TiO_2, Ti_2O_3, and Ti Metal by XPS, *Surf. Sci. Spectra* **1998**, *5*, 179-181.

5. Nakayama, M.; Xue, M.; An, W.; Liu, P.; White, M. G., Influence of Cluster-Support Interactions on Reactivity of Size-Selected Nb_xO_y Clusters. *J. Phys. Chem. C* **2015**, *119*, 14756-14768.

6. Bregante, D. T.; Priyadarshini, P.; Flaherty, D. W., Kinetic and spectroscopic evidence for reaction pathways and intermediates in olefin epoxidation on Nb in *BEA. *J. Catal.* **2017**, *348*, 75-89.

7. Reddy, G. R.; Balasubramanian, S.; Chennakesavulu, K., Zeolite encapsulated active metal composites and their photocatalytic studies for rhodamine-B, reactive red-198 and chloro-phenols. *RSC Adv.* **2015**, *5*, 81013- 81023.

8. Haber, F.; Weiss, J., Uber die Katalyse des Hydroperoxydes. *Naturwissenschaften* **1932**, *20*, 948-950.

9. Bakac, A., Physical Inorganic Chemistry: Principles, Methods, and Models. John Wiley & Sons: 2010; Vol.1, p. 134.

10. Ruddy, D. A.; Tilley, T. D., Kinetics and Mechanism of Olefin Epoxidation with Aqueous H_2O_2 and a Highly Selective Surface-Modified TaSBA15 Heterogeneous Catalyst. *J. Am. Chem. Soc*. **2008**, *130*, 11088-11096.

11. Wilson, N. M.; Bregante, D. T.; Priyadarshini, P.; Flaherty, D. W., Production and Use of H_2O_2 for Atom-Efficient Functionalization of Hydrocarbons and Small Molecules. *Catalysis* **2017**, *29*, 122-212.

12. Lin, W.; Frei, H., Photochemical and FT-IR probing of the Active Site of Hydrogenation Peroxide in Ti Silicalite Sieve. *J. Am. Chem. Soc.* **2002**, *124*, 9292-9298.

13. Bonino, F.; Damin, A.; Ricchiardi, G.; Ricci, M.; Spanó, G.; D'Aloisio, R.; Zecchina, A.; Lamberti, C.; Prestipino, C.; Bordiga, S., Ti-Peroxo Species in the TS-1/H_2O_2/H_2O System. *J. Phys. Chem. B* **2004**, *108*, 3573-3583.

14. Bordiga, S.; Damin, A.; Bonino, F.; Ricchiardi, G.; Lamberti, C.; Zecchina, A., The Structure of the Peroxo Species in the TS-1 Catalyst as Investigated by Resonant Raman Spectroscopy. *Angew. Chem. Int. Ed. Engl.* **2002**, *41*, 4734-4737.

15. Flaherty, D. W.; Iglesia, E., Transition-State Enthalpy and Entropy Effects on Reactivity and Selectivity in Hydrogenolysis of *n*-Alkanes. *J. Am. Chem. Soc.* **2013**, *135*, 18586-18599.

16. Wilson, N. M.; Flaherty, D. W., Mechanism for the Direct Synthesis of H_2O_2 on Pd Clusters: Heterolytic Reaction Pathways at the Liquid-Solid Interface. *J. Am. Chem. Soc.* **2016**, *138*, 574-586.